JOURNAL OF MATERIALS SCIENCE 30 (1995) 4930–4935

Structural and Raman analyses of the $(A_{1-x}Pb_x)TiO_3$ (A = Ca, Sr, Ba) perovskites

N. CALOS, J. FORRESTER*, T. J. WHITE†
Centre for Microscopy and Microanalysis, Queensland University, St Lucia, Queensland 4072, Australia

P. R. GRAVES, S. MYHRA‡
AEA Technology, Building 552.12, Oxfordshire OX11 ORA, UK

Powder X-ray diffraction and laser Raman spectroscopy were used to study systematically the structural and dynamical changes in three series of plumbous perovskites of composition $Ba_{1-x}Pb_xTiO_3Sr_{1-x}Pb_xTiO_3$ and $Ca_{1-x}Pb_xTiO_3$ with $0 < x < 1$. For the latter two series prominent phase transitions were found at x *ca.* 0.5 and 0.55, respectively. As well, Raman spectroscopy provided the means to track the evolution of active vibrational modes characteristic of the end-members across the doping range. The temperature dependence of the Raman spectra showed that the ferroelectric transition temperature of the (Ca, Pb) series can be tailored over a wide temperature range by judicious doping.

1. Introduction

Perovskite structures are ubiquitous and chemically diverse. They may be synthesized under a range of conditions and are important in such unrelated areas as core–mantle geology, refractory ceramics, waste management and electronics [1]. Many studies have been made of the crystallography of these compounds, with most emphasis having been placed on single crystal and powder X-ray diffraction. Fewer attempts have been made to use vibrational spectroscopic methods since the complexities of the spectra have tended to defy simple explanations. For example, McMillan and Ross [2] used Raman spectroscopy to study orthorhombic $CaBO_3$ perovskites with B = Ti, Ge, Zr and Sn. They concluded that no simple correlation could be made between the degree of orthorhombic distortion and the soft-mode behaviour evident from the spectra.

In this study, we report a comprehensive range of data from X-ray diffraction (XRD) and laser Raman microprobe (LRM) investigations on three solid solution series $Ba_{1-x}Pb_xTiO_3$, $Sr_{1-x}Pb_xTiO_3$ and $Ca_{1-x}Pb_xTiO_3$ with $0 < x < 1$. These perovskites are either cubic, tetragonal or orthorhombic, with symmetry changes which proceed smoothly as functions of composition. These specimens are ideal for monitoring subtle changes in the evolution of the Raman active vibrational modes, and to correlate these modes with structural changes.

2. Specimen synthesis

The $ATiO_3$ perovskites were prepared by solid state reaction using the following procedure. Stoichiometric amounts of $CaCO_3$ (99.99%), $BaCO_3$ (99.9%), $SrCO_3$ (99%), $PbCO_3$ (99%) and TiO_2 (99.9%) were ground and mixed thoroughly in an agate mortar and pestle. These mixtures were pressed into pellets of approximate dimensions of 10 mm diameter by 3 mm thickness. It was important to limit Pb volatilization during the firing. To accomplish this, excess material of the same chemical composition was placed in the base of an alumina crucible. This formed a bed for the pellets, which were then covered by more powder, and the crucibles were covered with a lid.

Each pellet was calcined in air at 600 °C for 12 h in order to partially dissociate the carbonates. The pellets were furnace cooled, removed from the furnace, crushed, sieved to 100 mesh and reformed into pellets. Different firing temperatures were chosen for each series of perovskites; this choice was based on the melting points of the calcine materials. For example, the (Pb, Ca)TiO_3 series was sintered at temperatures in the range 900–1200 °C, decreasing directly with the proportion of lead. The firing temperatures are summarized in Table I. The final firing lasted for 12 h and was followed by furnace cooling.

3. Characterization and analyses

3.1. XRD–Rietveld analysis

All the specimens, including the calcined material, were ground using an agate mortar and pestle, sieved to 200 mesh and then lightly pressed into ground-glass specimen holders. Data collection was repeated several times with freshly pressed samples in order to

* *Now at*: Department of Mining and Metallurgical Engineering, Queensland University, St. Lucia, Queensland 4072, Australia.
† *Now at*: Ian Wark Research Institute, University of South Australia, PO Box 1, Ingle Farm, South Australia 5098, Australia.
‡ *Visiting from*: Faculty of Science and Technology, Griffith University, Nathan, Queensland 4111, Australia.

0022–2461

TABLE I Temperature for final firing

Series	Temperature range (°C)
(Pb,Ca)TiO_3	900–1200
(Ba,Ca) TiO_3	1000–1200
(Pb,Sr)TiO_3	900–1500
(Pb,Ba)TiO_3	900–1000

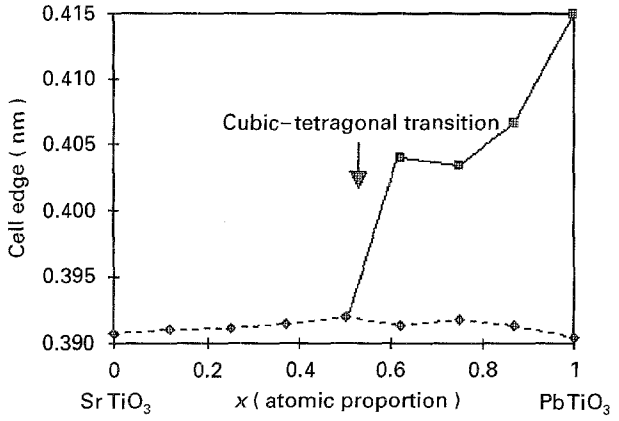

Figure 1 Refined cell parameters for the $Sr_{1-x}Pb_xTiO_3$ series as functions of x.—◆—, a_c or a_t; —▦—, c_t.

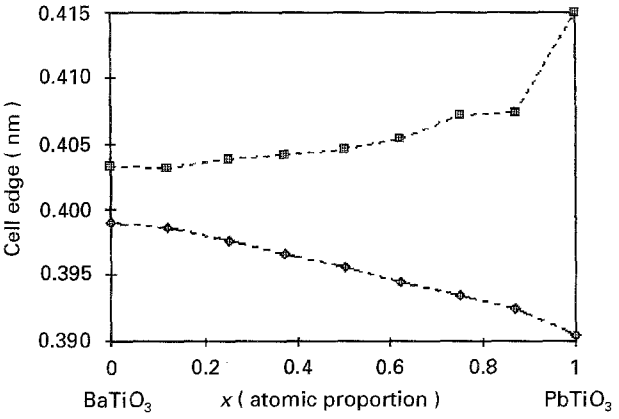

Figure 2 Refined cell parameters for the $Ba_{1-x}Pb_xTiO_3$ series as functions of x. —◆—, a_t; —▦—, c_t.

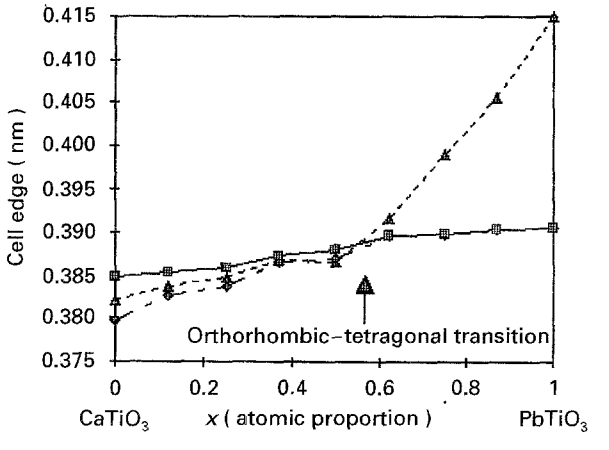

Figure 3 Refined cell parameters for the $Ca_{1-x}Pb_xTiO_3$ series as functions of x. —▦—, $a_0/\sqrt{2}$ or a_t; —△—, $b_0/2$ or b_t; —◆—, $c_0/\sqrt{2}$.

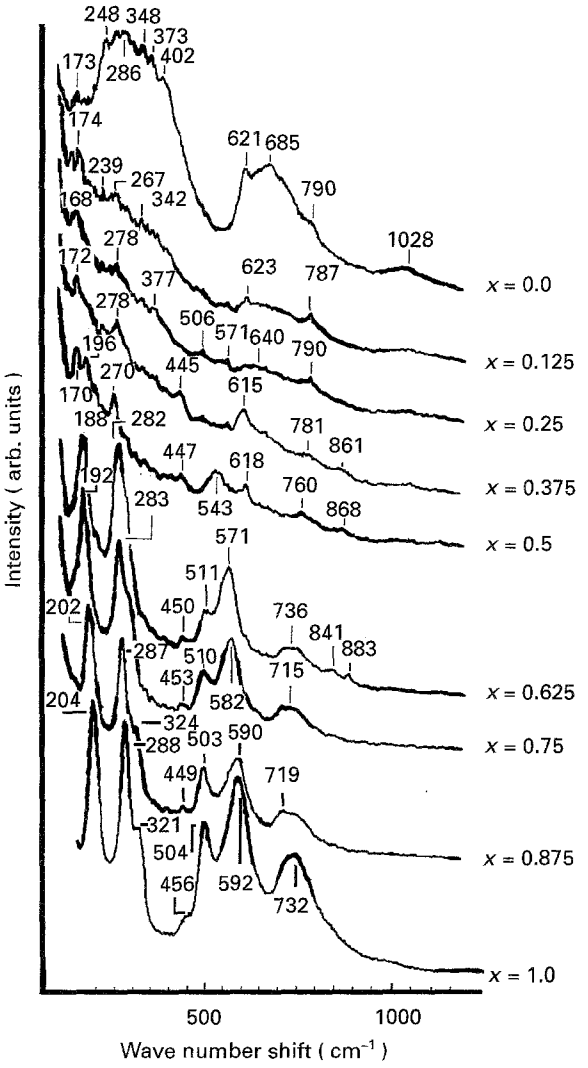

Figure 4 Raman spectra for the $Sr_{1-x}Pb_xTiO_3$ series as functions of x. The spectra have been normalized, but not otherwise processed.

ensure that the effects of preferred orientation were minimized. Diffraction data were collected at ambient temperature using a Siemens D5000 diffractometer operated in the step scanning mode. Following the procedures of Hill and Madsen [3], intensity measurements were made at intervals of 0.04–0.05° over the 2θ range 10–145° using unfiltered CuK_α radiation and 1° divergence and scattering slits. The X-ray source was operated at a power of 1.2 kW. All data sets were collected using a step counting time 5–15 s such that the strongest diffraction peak contained 2000–8000 counts.

Rietveld refinement of the data was carried out using the program developed by Wiles and Young [4], subsequently rewritten by Hill and Howard [5], and modified in-house to run on an IBM compatible personal computer. The background was defined by a four-parameter polynomial in $2\theta^n$, where n had values of 0–3. The diffraction profiles were fitted by a pseudo-Voight function in which the pseudo-Voight parameter, γ, was fitted to a polynomial $\gamma = \gamma_0 + \gamma_1 2\theta + \gamma_2(2\theta)^2$. A zero 2θ error was included in the refinement along with an asymmetry term developed to model axial divergence [5]. The peak width, H, was varied in accordance with $H^2 = W + V\tan\theta + U\tan^2\theta$ [6]. In addition, unit cell

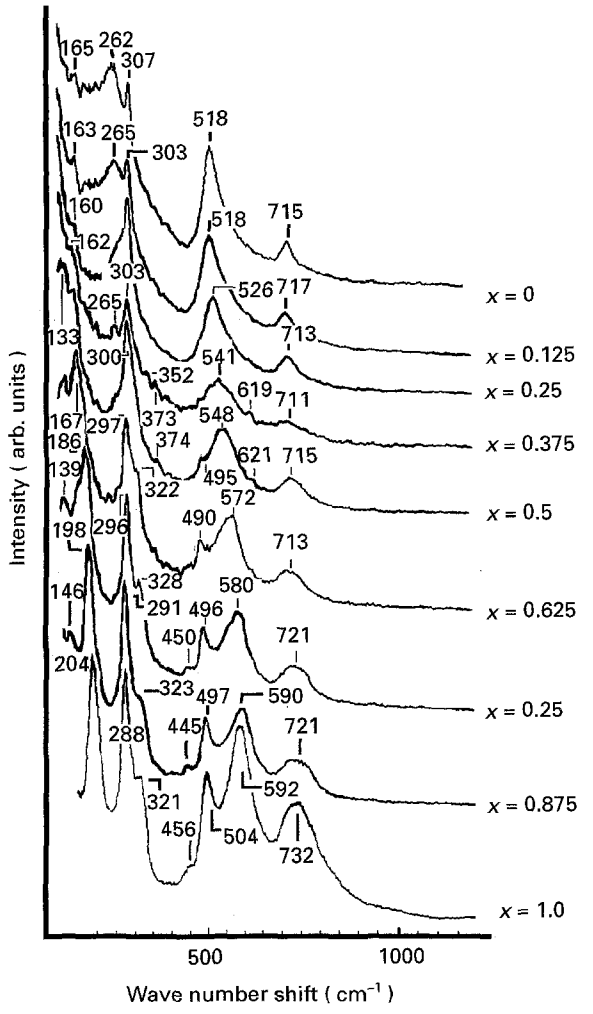

Figure 5 Raman spectra for $Ba_{1-x}Pb_xTiO_3$ series as functions of x.

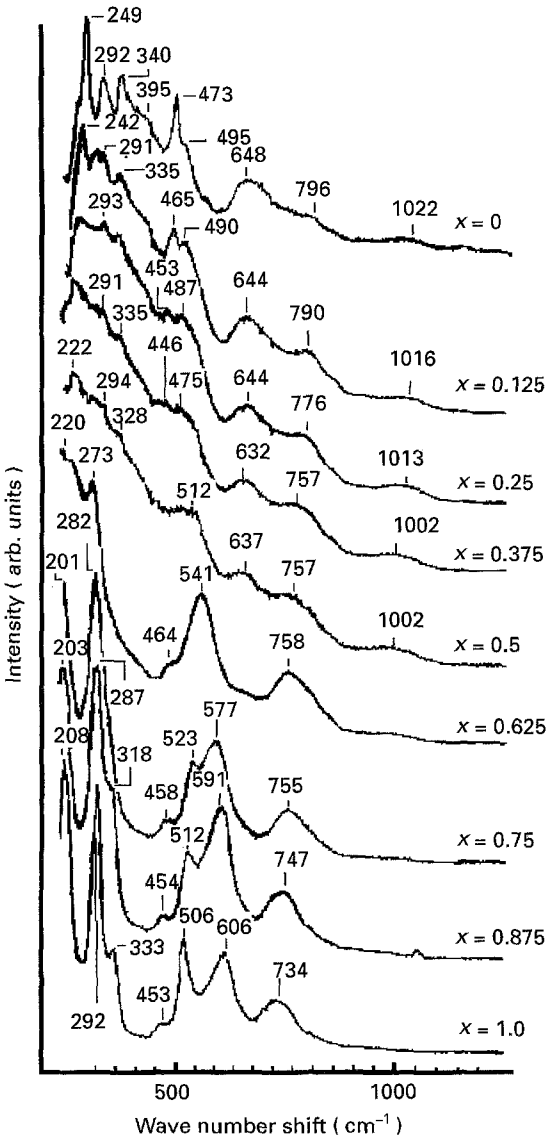

Figure 6 Raman spectra for $Ca_{1-x}Pb_xTiO_3$ series as functions of x.

parameters, scale factor, positional parameters and certain cation occupancies were refined. Generally, no attempt was made to refine isothermal vibration parameters which were arbitrarily fixed at 0.01 nm^2.

3.2. Raman analysis

The analyses were carried out with a laser Raman microprobe (LRM) with true backscatter configuration. The general features of the instrument have been described elsewhere [7], and the procedures were in accord with established practice (e.g. [8]). Parallel photon detection was effected with a two-dimensional liquid nitrogen cooled charge-coupled array–420 × 600 pixels–(AT1 CCD Imaging Systems, Wright Instruments, Ltd), with an overall quantum efficiency of 70%. Data acquisition was under computer control. The exciting source was the 514.5 nm line from an argon ion laser which was filtered by a pre-monochromator in order to remove unwanted plasma lines. The incident power was focused into a 2 μm spot using a 40× objective lens, and the backscatter collection efficiency was determined by its numerical aperture of 0.65. The incident power was limited to < 1 mW. As a result of the backscatter configuration for the LRM it was impossible to carry out measurements much below 150cm^{-1} wave number shift, due to the high intensity of elastically scattered radiation. Temperature-dependent measurements were carried out using a hot-stage (Stanton Redcroft HSM-5) with a UTP controller, resulting in a set-point stability of better than 1°C. The appearance of the high-temperature spectra (> 300 °C) suggests that black-body radiation from the cavity of the hot-stage became an increasingly important contribution to the background intensity. Room temperature measurements were made before and after each heating cycle in order to ascertain that the integrity of the specimens was unaffected by the heating.

4. Results

The refined cell parameters as functions of x, obtained from XRD and Rietveld analyses, are shown in Figs 1–3 for $Sr_{1-x}Pb_xTiO_3$, $Ba_{1-x}Pb_xTiO_3$ and $Ca_{1-x}Pb_xTiO_3$, respectively. In Figs 4–6 are shown montages of Raman spectra as functions of x for the same phases. For completeness, we also provide the Raman spectra for the $Ba_xCa_{1-x}TiO_3$ series in Fig. 7. Finally, Fig. 8 shows representative Raman data from the investigations of the temperature dependence of the active modes of the $Pb_xCa_{1-x}TiO_3$ series; the transition temperature is indicated in the figure. The

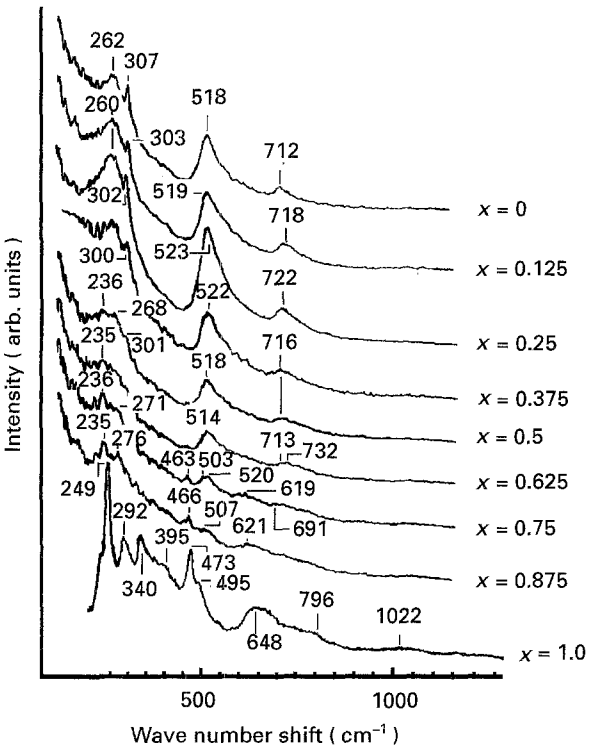

Figure 7 Raman spectra for $Ba_{1-x}Ca_xTiO_3$ series as functions of x.

outcomes of identifying the temperature of the phase transition for $1 \geqq x \geqq 0.5$ from the Raman spectra are shown in Fig. 9.

5. Discussion

5.1. The perovskite end-members

The end-members of the $A_{1-x}Pb_xTiO_3$ phases have been the subject of numerous structural investigations. Much useful information can be found in the excellent review by Galasso[9]; some of the data in the literature most relevant to the present work are summarized in Table II.

The Raman spectra of the ABO_3 compounds, when they exist in the ideal cubic phase, are dominated by strong second-order scattering, as evident in the case of $SrTiO_3$ with $Pm3m$ symmetry [8, 10]. The strength of the scattering is thought to be due to the large polarizability of the oxygen ion [11]. Distortions of the ideal structure, to tetragonality ($c/a \neq 1$) and to orthorhombicity ($a \neq b$, $c/a \neq 1$) result in a change in the size of the primitive unit cell. Accordingly, modes at the corners or edges of the first Brillouin zone of the cubic structure become Raman active. For instance, tetragonal $PbTiO_3$ have the following first-order active Raman modes [2] :

$$3A_{1g} + 4E_g + B_{1g} \quad (1)$$

However, orthorhombic $CaTiO_3$, according to Fately *et al.* [12], has the following Raman modes:

$$7A_{1g} + 7B_{1g} + 5B_{2g} + 5B_{3g} \quad (2)$$

Broadly speaking, there was good agreement in the case of the end-member phases between present results and those reported previously. The spectrum for $CaTiO_3$ compared well with those in the literature

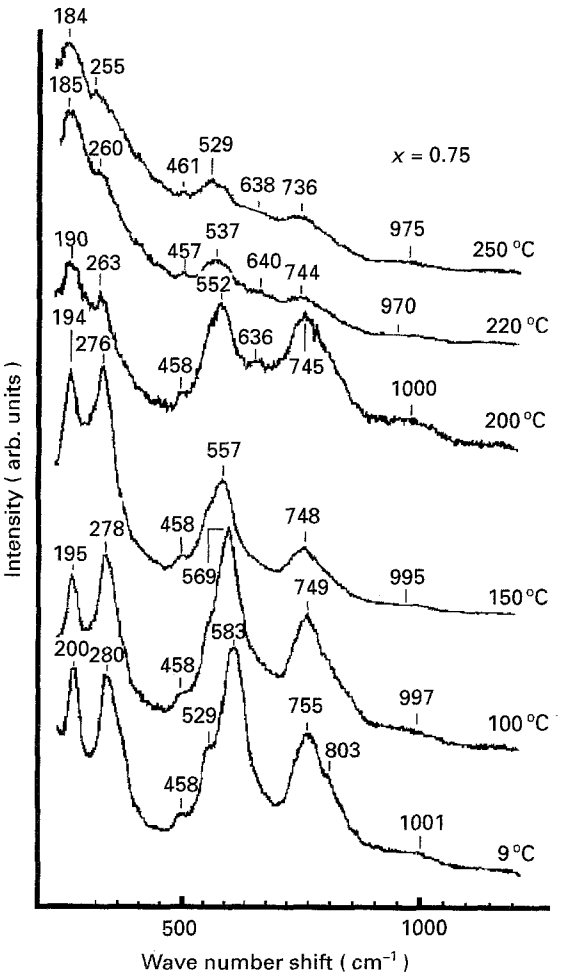

Figure 8 Representative results for the temperature dependence of the Raman spectra of the $Ca_{1-x}Pb_xTiO_3$ phases. The data for the $x = 0.75$ member are shown as an illustrative example.

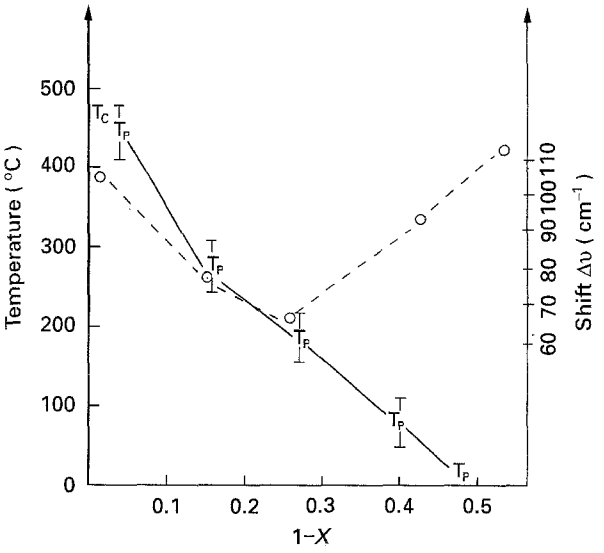

Figure 9 The change in the transition temperature (left ordinate and T_p symbols), as inferred from the temperature-dependent data for the $Ca_{1-x}Pb_xTiO_3$ series. Experimental uncertainties are indicated by the error bar. As well, the softening in the A_{1g} mode at 620 cm^{-1} (referred to the $PbTiO_3$ member) at the transition point has been plotted (right ordinate and O). T_c, known ferroelectric transition; T_p phase transition inferred from Raman.

[2, 8, 13]. Similarly, there was excellent agreement between the $SrTiO_3$ end-member spectrum in Fig. 4 and the results from other studies [8, 10, 14]. The present results for $PbTiO_3$ exhibited similar E_g modes to those

TABLE II Room temperature structural data for the $ATiO_3$ perovskites. These results are obtained from [9]

Phase	Symmetry	a	b	c	Phase transitions[a]
$BaTiO_3$	Tetragonal	3.989	3.989	4.029	$T_c = 393\,K$ $T_p = 183, 278$ K
$CaTiO_3$	Orthorhombic	5.381	7.645	5.443	$T_p = 870, 1270$ K
$SrTiO_3$	Cubic	3.904	3.904	3.904	$T_p = 110\,K$
$PbTiO_3$	Tetragonal	3.896	3.896	4.13	$T_c = 766\,K$

[a] T_c and T_p indicate ferroelectric and phase transitions, respectively.

TABLE III Summary of relevant information on the Raman active modes (from the literature)

$PbTiO_3$ [15]		$BaTiO_3$ [17]		$CaTiO_3$ [2,8,13]		$SrTiO_3$ [8,10,14]	
Shift	Character	Shift	Character	Shift	Character	Shift	Character
89	E_g	34	E_g			68	
130	E_g						
148	A_{1g}			155			
		183	E_g	175	B_{2g}/B_{3g}		
		189	E_g			200	
220	E_g			220		↑	
				241	B_{2g}/B_{3g}		
		270	A_{1g}	286	B_{2g}/B_{3g}		
		308	E_g	333	B_{2g}/B_{3g}		
362	A_{1g}						
440	E_g	466	E_g	468	B_{2g}/B_{3g}		Second
		471	A_{1g}				order
508	E_g	500	E_g	498	B_{2g}/B_{3g}		
		520	A_{1g}			550	
650	A_{1g}			620		600	
				↕	A_{1g}	↕	Second
		725	A_{1g}	690			order
						850	

reported in a recent study [15], while the A_{1g} modes (592 and 321 cm^{-1} in Figs 4–6) were shifted down by 40–60 cm^{-1}. A similar trend has been observed by Li *et al.* [16] for specimens subjected to heat treatment at less than optimum firing temperature. Finally, the present results for $BaTiO_3$ are in general agreement with those from two earlier studies [17, 18]; the distortion from the ideal cubic symmetry is relatively slight in this case and the A_{1g} and E_g modes are nearly degenerate.

The observed Raman features and inferred characters, reported in the literature, are summarized in Table III for the end-member phases at room temperature.

5.2. Evolution of Raman spectra for the $A_{1-x}A_xTiO_3$ series

5.2.1. $Ca_{1-x}Pb_xTiO_3$

The XRD results exhibit evolution from the orthorhombic end-member ($CaTiO_3$) via a near-"cubic" region ($0.25 \leqq x \leqq 0.5$) to a tetragonal phase (for $x > 0.5$). The correlations with the Raman spectra are excellent. For instance, it can be seen that the spectra for $x = 0.5$, 0.375 and 0.25 exhibit predominantly second-order character and are reminiscent of the spectrum of the $SrTiO_3$ end-member. Moreover, in the spectrum for $x = 0.625$, for which the tetragonal distortion is relatively slight and analogous to $BaTiO_3$, we see that the features are similar to those for the $BaTiO_3$ end-member. Also, it is apparent that the E_g modes at 450 and 508 cm^{-1} (in the $PbTiO_3$ end-member spectrum) "hardens" with decreasing x until they merge with the A_{1g} mode (located at 620 cm^{-1} in the $PbTiO_3$ end-member spectrum). This is consistent with the trend in the expansion of the c-axis dimension with increasing x. Conversely, the A_{1g} mode at 330 cm^{-1}, in the $PbTiO_3$ end-member spectrum, appears to "soften" with increasing x, and becomes more distinct with the approach to $x = 1$.

5.2.2. $Ba_{1-x}Pb_xTiO_3$

This series is characterized by the progression from the relatively slightly distorted ($c/a = 1.01$) $BaTiO_3$ tetragonal end-member, to the relatively more distorted ($c/a = 1.064$) $PbTiO_3$ tetragonal end-member. The overall structures of the spectra remain the same throughout the Ba ⇄ Pb substitution range. However, while A_{1g} and E_g modes are nearly degenerate in the $BaTiO_3$ end-member, this degeneracy is lifted with increasing x. At $x = 0.5$ the two types of modes are seen to emerge as resolvable entities. The E_g modes are seen to soften with increasing x, while the A_{1g} modes tend to harden by some 70 cm^{-1}. For instance, the 262 cm^{-1} A_{1g} mode ($BaTiO_3$) shifts approximately linearly with x to 321 cm^{-1} ($PbTiO_3$). Similarly, the 520 cm^{-1} A_{1g} mode ($BaTiO_3$) shifts to 600 cm^{-1}

($PbTiO_3$). These observations are in accord with the monotonic, nearly linear, changes in the lattice parameters with x, and are consistent with total solid solution solubility for Ba ⇆ Pb.

5.2.3. $Sr_{1-x}Pb_xTiO_3$

The principal features of this series are the abrupt cubic to tetragonal transition at $x = 0.5-0.6$, and that the prominent second-order structures in the cubic end-member phase are largely suppressed by doping with Pb. The latter is presumably due to the lack of long-range ordering of occupation on the A-site. The apparent emergence of first-order features of low intensity may be due to local ordering and small local distortions of the overall cubic structure. For $x > 0.5$ we find fully developed $PbTiO_3$-like spectra. The shifting of modes with increasing x is less pronounced in comparison with those for the two other Pb-based series, most likely because the abrupt increase in the c-parameter *vis-à-vis* the more gradual change for the two other series. However, there is a trend, some $20\,cm^{-1}$, toward harder A_{1g} modes with increasing x.

5.2.4. $Ba_{1-x}Ca_xTiO_3$

This series exhibits similar trends to those for the $PbTiO_3 \rightarrow CaTiO_3$ series. There is a gradual change from a tetragonal end-member ($BaTiO_3$) towards a near-cubic range for $0.625 \leqq x \leqq 0.875$, with an orthorhombic end-member ($CaTiO_3$) for $x = 1.0$. The $BaTiO_3$-like features remain intact over the range $0 \leqq x \leqq 0.625$; this suggests that Ca goes into $BaTiO_3$ in solid solution up to ca. 30 at % without affecting the structure.

5.3. Temperature dependence for the $Ca_{1-x}Pb_xTiO_3$ series

The temperature dependence of the Raman spectra for the members of the series which are tetragonal at room temperature shows that the temperature of the phase transition (766 K for the $x = 1$ end-member) is successively lowered by increasing Ca doping. The prominent A_{1g} mode at $620\,cm^{-1}$ in the $PbTiO_3$ member at room temperature softens with decreasing x and increasing temperature. The extent of the wave number shift at the transition temperature, from the $620\,cm^{-1}$ bench mark, has been plotted in Fig. 9, and shows a range of 70–$105\,cm^{-1}$, with a minimum of $70\,cm^{-1}$ for $x = 0.75$. The other modes are relatively less affected, exhibiting shifts of $< 15\,cm^{-1}$.

6. Conclusion

The present results demonstrate that the crystal structures of perovskites can be tailored across the ranges between the end-members of substitutional doping with A-site species. Of more technological relevance is the observation that the electronic structures, and in particular the paraelectric to ferroelectric transitions, will respond accordingly. Finally, we have shown that the laser Raman microprobe is a convenient non-destructive and sensitive tool for phase analysis of perovskite and related structures.

References

1. A. NAVROTSKY and D. J. WEIDNER (Eds.) "Perovskite: A structure of great interest in geophysics and materials science", Geophysics Monograph 45 (American Geophysical Union, Washington DC, 1989).
2. P. MCMILLAN and N. ROSS, *Phys. Chem. Minerals* **16** (1988) 21.
3. R. J. HILL and I. C. MADSEN, *Powder Diffraction* **2** (1987) 146.
4. D. B. WILES and R. A. YOUNG, *J. Appl. Crystallogr.* **14** (1981) 149.
5. R. J. HILL and C. J. HOWARD, *ibid. Appl. Cryst.* **18** (1985) 173.
6. G. CAGLIOTI, A. PAOLETTI and F. P. RICCI, *Nucl. Instrum.* **3** (1958) 223.
7. D. J. GARDINER, M. BOWDEN and P. R. GRAVES, *Phil. Trans. Roy. Soc. Lond.* **A320** (1986) 295.
8. P. R. GRAVES, S. MYHRA, K. HAWKINS and T. J. WHITE, *Physica C* **181** (1991) 265.
9. F. S. GALASSO, "Perovskites and high Tc superconductors" (Gordon and Breach, New York, 1990).
10. W. G. NILSEN and J. G. SKINNER, *J. Chem. Phys.* **48** (1968) 2240.
11. R. MIGONI, H. BILZ and D. BAUERLE, *Phys. Rev. Lett.* **37** (1977) 1155.
12. W. G. FATELEY, F. R. DOLLISH, N. T. MCDEVITT and F. F. BENTLEY, "Infrared and Raman selection rules for molecular and lattice vibrations: The correlation method" (Wiley-Interscience, 1972).
13. U. BALACHANDRAN and N. G. EROR, *Solid State Commun.* **44** (1982) 815.
14. *Idem., Commun. Am. Ceram. Soc.* (1982) **C54**.
15. M. D. FONTANA, H. IDRISSI, G. E. KUGEL and K. WOJCIK, *J. Phys. Condens. Matter* **3** (1991) 8695.
16. S. LI, R. A. CONDRATE and R. M. SPRIGGS, *Spectrosc. Lett.* **21** (1988) 969.
17. A. SCALABRIN, A. S. CHAVES, D. S. SHIN and S. P. S. PORTO, *Phys. Status. Solidi* (b) **79** (1977) 731.
18. A. PINCZUK, E. BURSTEIN and S. USHIOLA, *Solid State Commun.* **7** (1973) 139.

Received 6 June 1994
and accepted 5 April 1995